

# Emission-line profile modelling of structured T Tauri magnetospheres

Neil H. Symington, Tim J. Harries and Ryuichi Kurosawa

*School of Physics, University of Exeter, Stocker Road, Exeter EX4 4QL*

27 June 2018

## ABSTRACT

We present hydrogen emission line profile models of magnetospheric accretion onto Classical T Tauri stars. The models are computed under the Sobolev approximation using the three-dimensional Monte Carlo radiative-transfer code TORUS. We have calculated four illustrative models in which the accretion flows are confined to azimuthal curtains – a geometry predicted by magneto-hydrodynamical simulations. Properties of the line profile variability of our models are discussed, with reference to dynamic spectra and cross-correlation images. We find that some gross characteristics of observed line profile variability are reproduced by our models, although in general the level of variability predicted is larger than that observed. We conclude that this excessive variability probably excludes dynamical simulations that predict accretion flows with low degrees of axisymmetry.

**Key words:** accretion, accretion discs – line: profiles – radiative transfer – stars: circumstellar matter – stars: magnetic fields – stars: pre-main-sequence

## 1 INTRODUCTION

Classical T Tauri stars (CTTSs) are understood to be low-mass pre-main sequence stars accreting from circumstellar discs. Their spectra typically show emission lines of hydrogen and He I, and both permitted and forbidden metal lines (see e.g. Bertout 1989), while red-shifted absorption at high velocities (e.g. Edwards et al. 1994) suggests infall to the stellar surface. The basis for several models of the accretion process is a structured stellar magnetic field disrupting viscous disc transport near the Keplerian co-rotation radius. Gas is loaded onto the field lines and freefalls to produce hot impact regions at mid or high latitudes. Photospheric absorption line depths are diminished in comparison to those of similar main-sequence stars because of the veiling by excess continuum from the accretion hotspots. Magnetospheric accretion models are reviewed by Hartmann (1998).

The interaction between a stellar magnetic field and a disc can change the angular momentum evolution of the star. T Tauri stars usually rotate well below their break-up velocity despite accreting substantial amounts of material from a circumstellar disc. Details of the magnetospheres predicted by different models (e.g. Koenigl 1991, Shu et al. 1994) will have different effects on the stellar rotation period. Accretion from outside the Keplerian co-rotation radius can dissipate angular momentum to the disc, but gas from within the co-rotation radius will spin up the star. The requirement of a disc for this control mechanism (Collier Cameron & Campbell 1993,

Armitage & Clarke 1996) could be used to explain multiple populations of PMS stellar rotation rates (see e.g. Choi & Herbst 1996, Stassun et al. 1999, Hartmann 2002). Most models assume a dipole field configuration of order 1kG, although the finite radius over which the field must couple to the disc will introduce some distortion due to differential rotation on either side of the co-rotation radius. A more complex geometry with open magnetic field lines could launch the outflows (e.g. Shu et al. 1994; Paatz & Camenzind 1996) that are inferred from observations of blueshifted absorption. Johns-Krull et al. (1999) detected a 2kG longitudinal field component from a He I emission line in the spectrum of BP Tau, providing some evidence for ordered magnetic fields around CTTSs. Further observations (Valenti et al. 2003; Symington et al. 2005) found that the field strength of CTTS varied smoothly over consecutive nights and might be modulated by rotation of the system.

Hartmann et al. (1994) presented the first radiative transfer models of CTTSs with accretion occurring via an axisymmetric dipolar magnetic field structure, and it was found that the simulated hydrogen line profiles were successful in reproducing the gross characteristics of the observations. Improved models were presented by Muzerolle et al. (1998) and Muzerolle et al. (2001), incorporating line damping and extending the statistical equilibrium calculation of the hydrogen atom to 20 levels. These developments led to better quantitative agreement with the observed line profiles, to the extent that the model has subsequently been used to derive mass-accretion rates from H $\alpha$  ob-

servations (e.g. Muzerolle et al. 2003; Bouvier et al. 2003; Lawson et al. 2004).

Despite these successes, it is clear that the circumstellar geometry around a typical CTTS is far from a static, axisymmetric, dipolar inflow. For example, monitoring of six CTTSs over five nights (Smith et al. 1999) revealed permitted line profile variability attributed to rotation (time-scales of days), variable accretion (several hours), and flaring (about an hour). It was found that the  $H\gamma$  and  $H\delta$  line profile variability was strongly correlated but that there was a time delay between variations in the high-excitation lines and those from lower-energy lines. Hourly variations seen in RU Lup by Stempels & Piskunov (2002) are attributed to varying mass accretion rates and/or changes in the distribution of accreting matter. Those authors conclude that the observations rule out an axisymmetric accretion flow from a disc aligned perpendicular to the stellar rotation axis. A spectroscopic and photometric study of AA Tau (Bouvier et al. 2003) revealed a time delay between variations in the  $H\alpha$  and  $H\beta$  profiles and the veiling continuum. It was argued that this lag was the result of a change in accretion rate propagating (in freefall) along the field lines, with the change in density being observed first in the line profiles and then in the continuum when the increased kinetic energy of the flow is liberated at the hot spots.

Variability is often observed on rotational time-scales. Johns & Basri (1995b) obtained optical time-series spectra of SU Aur and found variations in the red-shifted absorption component of  $H\beta$  on the same time-scale as the stellar rotation period. A blue-shifted absorption feature consistent with an outflow was found to be anti-correlated with the red-shifted inflow signature, suggesting a magnetosphere that is seen to alternately favour inflow then outflow at different rotational phases. Petrov et al. (1996) also found evidence for simultaneous outflow and infall in SU Aur (Balmer lines and  $He\ I\ 5876\text{\AA}$ ). The possibility of an offset dipolar accretion structure was considered, but the complex kinematics of the magnetically channelled gas and the degeneracy of the observational diagnostics make quantitative conclusions difficult to achieve.

Long-term monitoring of CTTS TW Hya (Alencar & Batalha 2002) revealed evidence for both inflow and outflow in the Balmer line profiles, with the deepest  $H\alpha$  blueward absorption occurring at phases when the veiling continuum (and hence mass accretion rate) is greatest. It was suggested that the system is viewed at low inclination, although the presence of photometric variability argued against a truly face-on orientation. A similar viewing angle was used to explain the redwards peaked Balmer line profiles of DR Tau (Alencar et al. 2001).

Oliveira et al. (2000) performed cross-correlation analysis of multiple spectral lines from SU Aur to investigate non-coincident changes. Different components of line profiles were seen to be time-lagged with respect to each other, which is inconsistent with the expectation for a simple geometry. It was suggested that the accretion flow had an azimuthal component and that the observer's line of sight was sampling different different physical environments for line formation. Structured accretion is also supported by the observations of VZ Cha (Smith et al. 2001) who report features that persist for longer than the likely freefall time from the inner edge of a truncated disc. The possibility of confinement to two

rotating streams was considered, with the observed period being only half the stellar rotation period.

If we are to fully understand the magnetospheric accretion process, from its role in rotational breaking to the use of line profiles as accretion diagnostics, we must obtain a better description of the geometry of the circumstellar flows. The observational evidence for structured accretion is overwhelming, and it is now appropriate to challenge these data with theoretical models. In this paper we present the first 3D radiative-transfer modelling of azimuthally-structured accretion. We note that it is not the aim of this work to reproduce in detail the variability of permitted line profiles in CTTS, but rather to gain insight into the likely characteristics of line profile variability that would be produced by 'cartoon' geometries that have been invoked by other researchers to interpret their timeseries data. As a first step we adopt a canonical, bipolar reference model, and examine the synthetic line profiles produced by simple departures from axisymmetry in the magnetosphere.

## 2 RADIATIVE TRANSFER MODELLING

We have extended the TORUS radiative-transfer code (Harries 2000) in order to simulate hydrogen line profiles from pre-main-sequence stars with magnetospheric accretion flows. The circumstellar environment of accreting T Tauri stars encompasses a large range of length scales. Assuming that the material is strongly influenced by the magnetosphere, we must consider a volume extending to several stellar radii from the surface. The addition of a disc (or a large-scale outflow) will further enlarge the space in which our simulated photons may have significant interactions. Close to the stellar surface, the magnetic fields may confine gas in narrow columns, leading to small impact regions at the photosphere. The liberation of energy by shock heating by the infalling gas in these areas may be the source of much of the system's luminosity.

The complexity of the circumstellar environment requires a careful choice of mapping to the simulation's grid. Regular subdivision of our model space (e.g. in spherical polar coordinates) leads to many of the cells representing regions with little effect on the radiation field. By adopting the technique of adaptive mesh refinement (AMR) we can tailor the subdivision of the simulation space to improve the sampling of the structures it contains (see e.g. Kurosawa & Hillier 2001; Steinacker et al. 2003; Harries et al. 2004; Kurosawa et al. 2004). Our whole cube-shaped space is divided into eight, smaller cubic subcells; and those subcells are themselves repeatedly divided until some criterion is satisfied throughout the grid. For the models presented in this paper, we specify the maximum mass that any subcell can contain. This rule can be applied efficiently if we can quickly calculate the density at any location within the grid; and it concentrates many small subcells where gas is present, while the empty regions are only sampled by a few large cells. Symington (2005) gives further details of our AMR implementation.

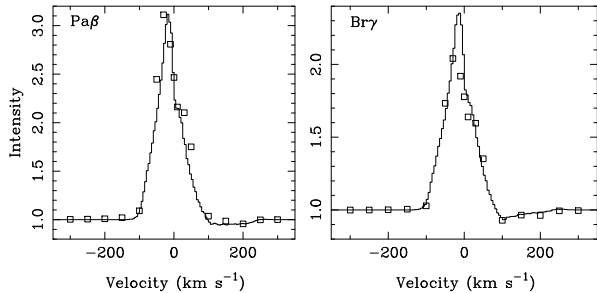


**Figure 1.** Hydrogen line profiles for an axisymmetric accretion geometry with parameters:  $\dot{M} = 10^{-7} M_{\odot} \text{ yr}^{-1}$ , accretion stream  $T_{\text{max}} = 7000\text{K}$ ,  $R_{*} = 2R_{\odot}$ ,  $M_{*} = 0.5M_{\odot}$ , viewing inclination =  $30^{\circ}$ . The accretion stream begins in the disc plane between  $r_{\text{inner}} = 2.2R_{*}$  and  $r_{\text{outer}} = 3.0R_{*}$ . Solid line: TORUS 3-D computation with AMR scheme. Squares: MCH computation (reproduced from <http://cfa-www.harvard.edu/cfa/youngstars/>)

## 2.1 Accretion flow model

In order to investigate the effect of azimuthal structure on the line profiles we must adopt a reference model for the circumstellar geometry. Here we use the model of an accretion disc and stellar magnetic field given by Hartmann et al. (1994, hereafter HHC), in which a dipole magnetic field intersects the disc and allows gas to free-fall along the field lines to the stellar surface. The pressure of the gas picked up from the disc is assumed to cause no distortion of the magnetic field, and the innermost field line defines the radius where the disc is completely truncated. The density and velocity at any point in the flow can be computed directly from the analytical formulae of HHC, which are based on the conservation of mass and energy. We have not attempted to include rotation of the magnetosphere in our model. This simplification may slightly change the central peak of our simulated line profiles (dominated by low velocity gas near the disc), but should not affect the line wings (see Muzerolle et al. 2001, hereafter MCH). Although not as sophisticated as using a Shu-type magnetosphere (Shu et al. 1994), or indeed adopting the density structure from an MHD simulation (e.g. Romanova et al. 2003), this is the simplest, plausible circumstellar structure, and it enables us to easily investigate the effect of departures from axisymmetry on the emission lines.

Upon reaching the stellar surface, shock heating of the infalling gas will liberate its kinetic energy. We adopt the assumption of HHC that the radiation (typically X-rays) is immediately reprocessed and all the accretion energy is radiated from the impact region as a blackbody. The geometry and mass-transfer rate of our accretion flow (both of which quantities may vary with time) define the pattern of hot-spots over the stellar surface. At each temporal phase in our simulations we calculate the kinetic energy of the flow directly above a grid of points distributed over the stellar surface. Ignoring any heating/cooling time-scale, we specify the emitted spectrum of each surface element to be the sum of the intrinsic stellar spectrum and a blackbody contribution from the instantaneous local accretion rate. The time-independent accretion models presented in this paper create hot-spots with temperature  $\sim 7250\text{K}$ .

Perhaps the greatest uncertainty in the magnetospheric

radiative-transfer modelling to date is the temperature structure of the accretion flow. The form of the temperature run will have a significant impact on the line source functions, and hence the line profiles themselves. To our knowledge the only study to address this aspect explicitly is the work of Martin (1996). He calculated the temperature structure of dipolar accretion flows with the same geometry and density as HHC. Heating was found to be dominated by adiabatic compression as the magnetic field lines converge along the path of the flow, while the major coolants were bremsstrahlung radiation and line emission from Ca II and Mg II. He found that the temperature of the accretion flow grew from the disc, and reached peak temperatures of  $\sim 6000\text{K}$  before the temperature fell as the density (and hence the cooling) increases towards the stellar surface. For the purposes of this paper, in which we are concentrating geometrical effects, we have adopted the temperature profile of HHC (see fig. 6 in their paper), which qualitatively matches the Martin (1996) results. We defer studying departures from this temperature law to future work, but note that multi-line spectral analysis of observations should provide strong constraints on the magnetospheric temperatures.

The statistical equilibrium code is based on STATEQ (Harries 1995), an implementation of the method of Klein & Castor (1978). The radiation field is computed by integrating the spectrum from each surface element of the star, weighted by the solid angle subtended from the centre of a grid cell. We typically take advantage of any symmetries present in our models to increase the computational efficiency. For example, for axisymmetric accretion flows, we can initially calculate the statistical equilibrium for grid cells in a plane, and then rotationally map the solution characteristics to the other cells. The iterative calculations for all of the cells throughout the 3D grid will then proceed quickly because they are starting close to the solution they will converge upon. We compute the first 14 levels of the hydrogen atom in order to have sufficient high- $n$  levels to avoid the inevitable overpopulation of levels near the continuum impacting on the upper levels of the lines under consideration.

## 2.2 Monte Carlo radiative transfer

The radiative transfer algorithm is described in Harries (2000) with reference to a spherical polar grid. We have updated the implementation to use recursive routines so that it can be applied to our AMR grid, which is stored in a tree structure. The emissivity of each grid cell in the flow region is used to weight the probability of that cell being the source of a Monte Carlo photon. The stellar photosphere is separately represented by a grid of small surface elements. Photons originating from the star are weighted by the continuum luminosity of each element at the wavelength of the spectral line.

The numerical integration from the source of a photon to the observer is described in Harries (2000). Sampling of the conditions along each photon's path is done with a recursive traversal of the tree structure storing the AMR cells. The line transfer is performed under the Sobolev approximation, and we neglect non-local coupling terms (which would render our 3D calculations computationally intractable). Both assumptions lead to a negligible effect in the line wings, but may have a significant impact at the line core. Addi-

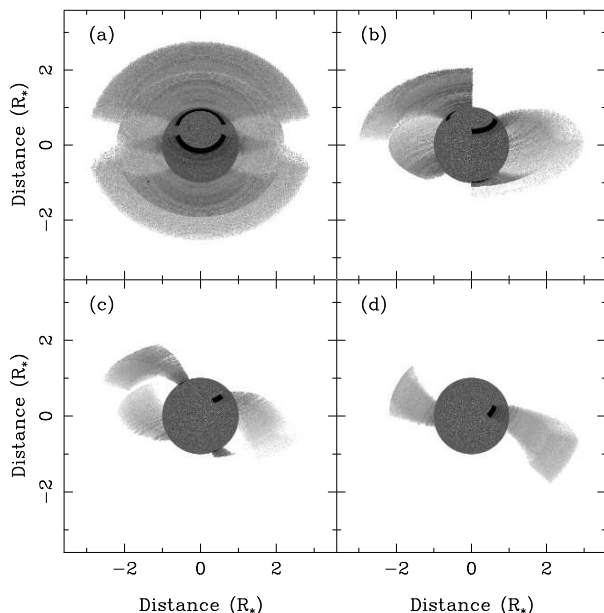


**Figure 2.** The four accretion models (see Table 1): (a) D150 (b) D90 (c) D30 (d) A30. The observer views the systems at inclinations of  $30^\circ$  (a and d) or  $60^\circ$  (b and c). The intensity is measured over a narrow wavelength band around the  $H\alpha$  line ( $6550\text{--}6575\text{\AA}$ ). The accretion footprints are obvious as bright hotspots at high latitudes. The images are logarithmically-scaled over three decades from most intense (black) to least intense (white). The opaque accretion discs truncate the view of the accretion stream(s) below the disc planes.

tionally, we do not include the effects of line damping. Our model profiles are therefore likely to underestimate the true extent of the line breadth for  $H\alpha$  (see MCH for a discussion and comparison of results) but will have little effect on the higher order lines.

Alfen-driven turbulence has been invoked to explain the broad, symmetric wings that are observed in some profiles (e.g. Decampoli 1981; Hartmann et al. 1982; Basri 1990; Alencar & Basri 2000). We have not included turbulent broadening in the calculations presented here, since if the velocity amplitude of the turbulence is comparable with the bulk flow velocity then the Sobolev approximation breaks down. As we are interested in the imprint of geometrical structure on the emission line profiles we do not regard the lack of turbulent broadening in our models as a significant problem, and furthermore we note that its inclusion requires co-moving statistical equilibrium calculations in three-dimensions, a problem that is computational intractable at present.

We choose to present our synthetic spectra normalized to the local continuum at each time interval. We do not correct for veiling of absorption features or suppression of emission features by a changing continuum level. While observations of comparable spectra can compensate for these effects (e.g. Edwards et al. 1994), these corrections introduce their own uncertainties and many authors present spectra without such processing (Alencar et al. 2001; Smith et al. 2001).

### 2.3 Code testing

We have performed numerical tests to ensure the spatial resolution of our simulations (typically based on  $\sim 10^6$  grid cells) is sufficient to represent the accretion flow geometry we are using. In Fig. 1 we compare  $\text{Pa}\beta$  and  $\text{Br}\gamma$  profiles (selected to minimize discrepancies due to line damping) computed in 3D using TORUS with the profiles for the same geometry calculated using the code described by MCH. Given the slightly different physics underlying the two codes the profiles show satisfactory agreement in intensity and morphology.

The Monte Carlo radiative transfer data sets presented later have each been generated from at least  $1 \times 10^6$  photon packets. The noise correlation between our spectral wavelength bins, and our adoption of many variance-reduction techniques, prohibits simple estimation of the effective signal-to-noise ratio, but the excellent reproducibility of our results suggests noise is insignificant.

### 2.4 Accretion models

Time-series observations of the line profile variability of CTTs have not yet provided unambiguous clues to the structure of the accretion flows. The observer is likely seeing a geometry with overall characteristics persisting for longer than the rotational time-scale, but with some structure varying more rapidly. The accretion rate is also expected to show changes on short time-scales dependent on the changing magnetic field configuration (Smith et al. 2001).

In this paper, we aim to identify some of the characteristics of the magnetically-controlled accretion. If, in one simulation, we depart in too many ways from the simple steady-state models it will be difficult to identify the contributions from each change. We have therefore made only small adaptations to the HHC magnetospheric accretion geometry, breaking the axisymmetry to investigate line profiles as the star rotates. The accretion flows are confined to two azimuthal curtains around the star so that their projection against the stellar disc and hot-spots changes during a rotation cycle. This scenario was suggested by Smith et al. (2001) as an explanation for the periodicity in the spectra of VZ Cha.

This configuration also is similar to that found in the 3D MHD simulations of Romanova et al. (2003). Those authors model a magnetic field slightly inclined relative to the star's rotation axis and the disc plane. Accretion is energetically favourable at some azimuth positions, and the flow becomes concentrated in two streams (see fig. 5 of their paper). We have simulated accretion curtains which are symmetric about the disc plane, and also streams that are diametrically opposite about the star.

Romanova et al. (2003) found that the accretion was axisymmetric in the case where the magnetic and rotation axes were the same. For one of our non-axisymmetric models, we have therefore implemented an offset between these two axes. The HHC formulation for the accretion flow would not represent such a misalignment without substantial reworking. We have instead used the HHC accretion flow unmodified, and achieved the offset effect by only changing the rotation axis for our simulated observations, and the disc axis. The start of the accretion flow is then not coincident

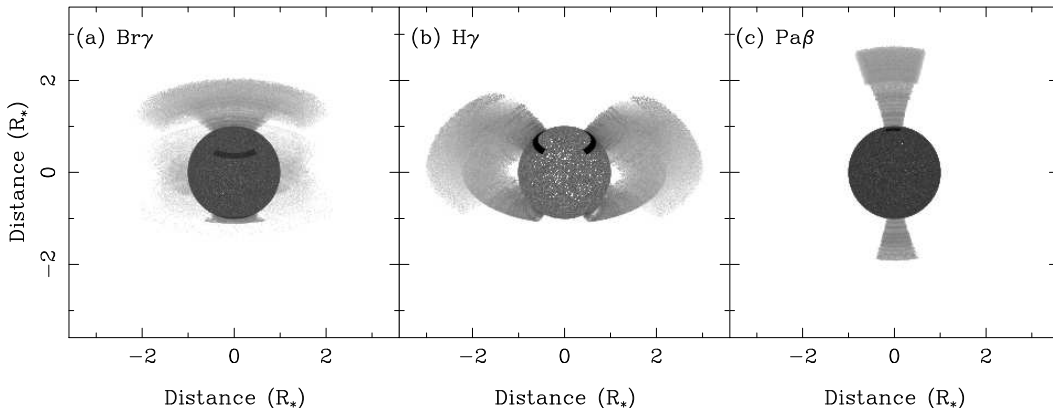


**Figure 3.** Intensity images of accretion models at selected phases. Each image shows flux integrated over a narrow wavelength range (corresponding to  $\pm 500 \text{ km s}^{-1}$ ) around the rest wavelength of the indicated spectral line. (a) D90 viewed at the wavelength of  $\text{Br}\gamma$  at phase 0 ( $60^\circ$  inclination). The two streams lie directly in front and behind the star. (b) A view of D90 at phase 0.25 ( $\text{H}\gamma$  passband,  $60^\circ$  inclination). The streams are perpendicular to the line of sight. (c) A30 at  $\text{Pa}\beta$  at phase 0.5 ( $30^\circ$  inclination). The lower stream is towards the observer but viewed through the disc’s inner hole and so appears truncated. The upper stream is on the far side of the star – the accretion hotspot is marginally visible at the limb. The images are logarithmically scaled over four decades, from black (most intense) to white (least intense).

**Table 1.** Model parameters and properties of the spectral continua. Double accretion curtains are mirrored about the disc plane, while the alternate configuration has one stream above the disc, and one below, at opposing azimuth angles. These models are illustrated in Fig. 2. The mean levels are quoted for an observer at a distance of 100 pc. The range is the full range of the continuum variability, expressed in magnitudes. The final column gives the relative contribution to the continuum flux from the accretion hotspot ( $f_{\text{acc}}$ ), relative to the photospheric flux ( $f_{\text{phot}}$ ) at the line wavelength.

Model	Accretion curtains		$\dot{M}$	Magnetic offset	Line	Inc.	Mean continuum	Range	$f_{\text{acc}}/f_{\text{phot}}$
	Type	Angular size	( $M_\odot \text{ yr}^{-1}$ )				( $\text{erg s}^{-1} \text{ cm}^{-2} \text{ \AA}^{-1}$ )	(mag)	
D150	Double	$150^\circ$	$8.3 \times 10^{-8}$	$0^\circ$	$\text{H}\gamma$	$60^\circ$	$3.9 \times 10^{-13}$	0.06	3.9
D90	Double	$90^\circ$	$5.0 \times 10^{-8}$	$0^\circ$	$\text{H}\gamma$	$30^\circ$	$3.7 \times 10^{-13}$	0.0	2.3
						$60^\circ$	$2.7 \times 10^{-13}$	0.15	
					$\text{H}\alpha$	$60^\circ$	$3.4 \times 10^{-13}$	0.07	0.58
					$\text{Pa}\beta$	$60^\circ$	$1.7 \times 10^{-13}$	0.03	0.16
					$\text{Br}\gamma$	$60^\circ$	$5.7 \times 10^{-14}$	0.002	0.08
D30	Double	$30^\circ$	$1.7 \times 10^{-8}$	$0^\circ$	$\text{H}\gamma$	$60^\circ$	$1.5 \times 10^{-13}$	0.14	0.78
A30	Alternate	$30^\circ$	$8.3 \times 10^{-9}$	$10^\circ$	$\text{H}\gamma$	$30^\circ$	$1.3 \times 10^{-13}$	0.3	0.38
					$\text{H}\alpha$	$30^\circ$	$2.5 \times 10^{-13}$	0.13	0.096
					$\text{Pa}\beta$	$30^\circ$	$1.5 \times 10^{-13}$	0.04	0.026
					$\text{Br}\gamma$	$30^\circ$	$5.3 \times 10^{-14}$	0.03	0.013

with the surface of the disc, but the results are approximately valid for small angular offsets (we choose  $10^\circ$ ).

We adopt the CTTS system parameters of HHC:  $M_* = 0.8M_\odot$ ,  $R_* = 2R_\odot$ ; and an accretion stream beginning close to the disc plane between  $r_{\text{inner}} = 2.2R_*$  and  $r_{\text{outer}} = 3.0R_*$ . The stellar continuum flux is described by a model atmosphere for  $T_{\text{eff}} = 4000\text{K}$ ,  $\log g = 3.5$  (Kurucz 1993). The mass accretion rate *per unit azimuth angle, per hemisphere* is the same in each case (integrating to  $10^{-7}M_\odot \text{ yr}^{-1}$  if the accretion streams were complete), but the limited extent of the flow in each model reduces the effective accretion rate. Table 1 shows the parameters that differ between the models. We have simulated line profiles at viewing inclinations measured with respect to the stellar *rotation* axis.

### 3 RESULTS

The results we present are grouped to demonstrate the effects of changing individual aspects of the simulation (spectral line, accretion geometry and viewing inclination). For two of the models, we show time-series spectra simulated for four spectral lines (Sections 3.1 and 3.4). We also compare the spectra for a single line ( $\text{H}\gamma$ ) as the accretion geometry or viewing inclination are altered (Sections 3.2 and 3.3 respectively).

#### 3.1 Spectral line comparison

The D90 model has accretion streams on opposite sides of the star, both above and below the disc, i.e. four in total (Figs. 2b, 3a, 3b). Each stream covers an azimuth range of  $90^\circ$ , and the whole system is viewed from an inclination of  $60^\circ$ . At this angle, the upper accretion hotspots alternately rotate out of the line of sight, modulating the observed con-

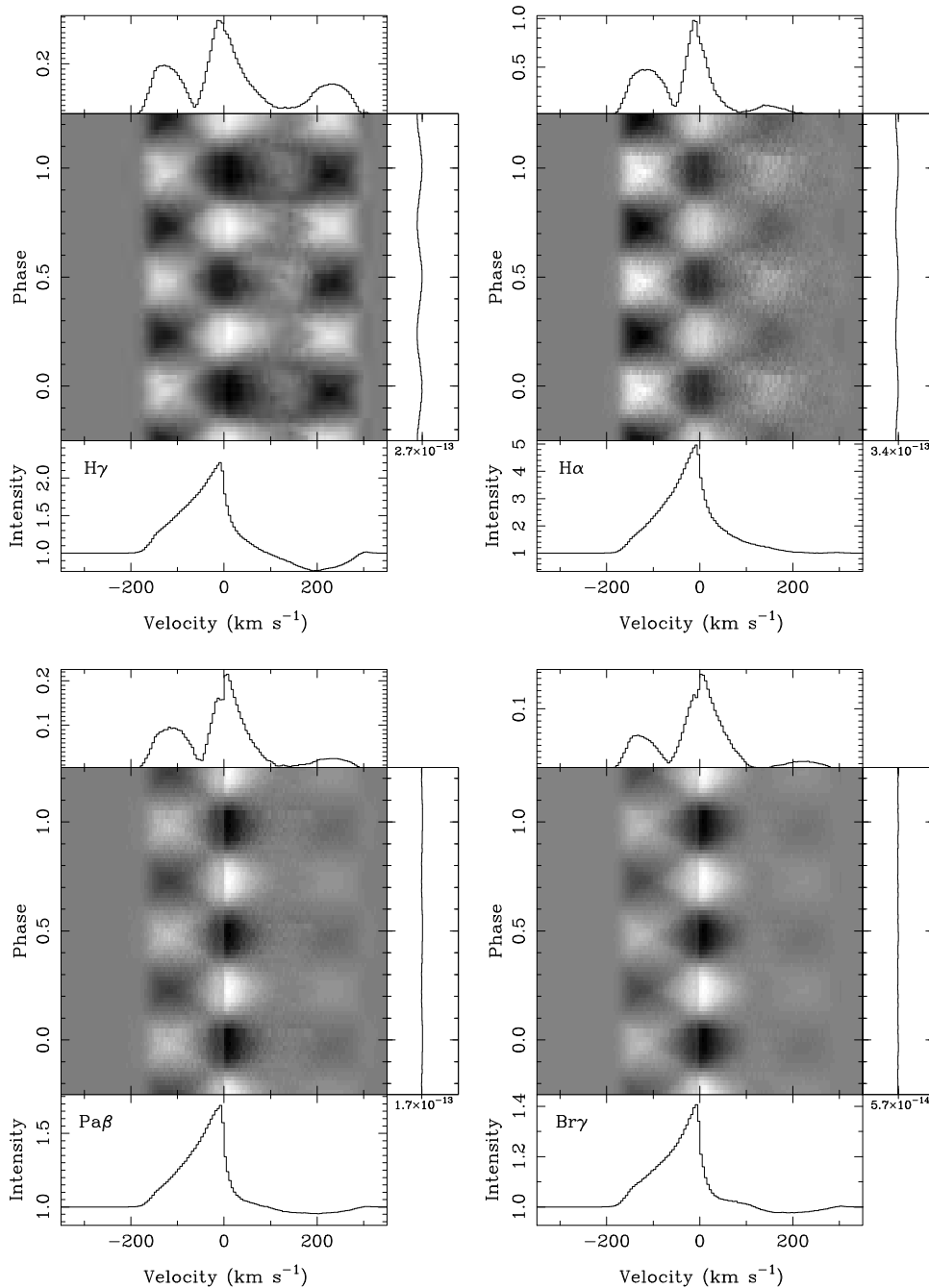


**Figure 4.** Spectra from D90 model, viewed at  $60^\circ$  inclination. The bottom plots show the mean spectrum for each hydrogen line. The greyscale image shows the quotient of the spectrum at each rotational phase, with respect to the mean spectrum. The variability shown in the greyscale has ranges (from top left) of 57, 79, 47 and 35 per cent of the mean spectrum in a given wavelength bin. The plot beside each greyscale image shows the continuum level at each phase – the scales are presented in Table 1 and the values increase towards the right hand side. The RMS deviations of each wavelength bin are plotted in the uppermost box, with the zero point at the bottom of the box.

tinuum intensity (Fig. 4; Table 1). This effect is most pronounced (0.15 mag) at the wavelength of the  $H\gamma$  line because the hotspots contribute most significantly to the blue continuum.

The hydrogen line profiles show periodic variations as the projected velocity of the inflowing streams changes over a rotational period (Figs. 4, 5a). The mean spectral profiles are all peaked at the rest wavelength of the line and are

asymmetric with most of the emission occurring blueward of line centre.  $H\alpha$  is the strongest of the lines and is in emission over its full width; the others all show inverse P Cygni profiles, with  $H\gamma$  having the most significant red-shifted absorption feature. The origins of the line profile shapes are found in the line source functions (Fig. 6). The source functions of all four lines lie below their local Planck functions, although the lines become more thermalized as the density increases

rapidly close to the stellar surface. For  $H\gamma$  and the near infrared transitions, the line source functions are significantly smaller than the Planck function for a  $T \sim 7250\text{K}$  continuum source: an IPC profile therefore results when the hot spots are viewed through the intervening accretion streams. The  $H\alpha$  source function is significantly more thermalized, and does not show red-shifted absorption.

Observers often present the temporal variance spectrum (TVS) of their line profile timeseries (e.g. Johns & Basri 1995a; Oliveira et al. 2000), and it is a useful diagnostic for quantifying both the level and velocity distribution of line profile variability. In Fig. 4 we present the root-mean-square (RMS) spectra of our models, which is a comparable diagnostic to the TVS. It is immediately apparent that the  $H\alpha$  model shows the strongest variability, and that all lines show a multiply-peaked RMS spectrum with the highest variability occurring at line centre.

The  $H\gamma$  profile varies at three velocity ranges, two of which are well correlated with each other (seen in the RMS plot as bands centred at 200 and  $0\text{ km s}^{-1}$ ); and the other is anticorrelated with those two (seen at  $\sim -130\text{ km s}^{-1}$ ). There are two regions between these bands which are almost invariant because the integrated line emission seen at some velocities remains constant throughout the rotation period.  $H\alpha$  shows the same zero-velocity and blueshifted bands, but the high-velocity red-shifted band is constant ( $H\alpha$  does not show an IPC absorption feature). In the two infrared lines, the red-shifted and blue-shifted emission is less variable than for  $H\gamma$ , but the line centre still shows large changes in intensity. The maximum of the low-velocity component occurs at phases 0.25 and 0.75 when the streams are perpendicular to the line of sight, and the projected velocity of the inflowing gas is minimized (Fig. 3b). At these phases, all the line profiles (Figs. 4, 5a) are composed of a symmetric emission peak around  $0\text{ km s}^{-1}$ , and (excepting  $H\alpha$ ) a small red-shifted absorption feature (only a very small volume of gas is seen in front of the hot-spot with this configuration).

Phases 0 and 0.5 (Figs. 3a, 5a) have the streams aligned with the observer, and the projected velocities of the gas are maximized. Considering first  $H\gamma$ , the stream in front of the star is responsible for strong absorption at  $\sim +220\text{ km s}^{-1}$ . Blueward of line centre is a broad flat-topped emission feature extending to  $\sim -170\text{ km s}^{-1}$ . The line profile variability in the red line wing is strongest for  $H\gamma$ , since the hot spot emission (which is dominant at short wavelengths) is absorbed by the infalling material. The red-wing variability is considerably smaller for the other transitions, mainly due to the smaller contribution of the hot-spots to the total continuum flux.

### 3.2 Geometry comparison

Our second group of results (Fig. 7) are all for the  $H\gamma$  line observed from an inclination of  $60^\circ$ , and we show synthetic spectra for accretion streams with different azimuthal extents. The mean spectrum for the D90 model is shown with the other two mean spectra (after rescaling to equal equivalent widths) for comparison, and the lines have almost the same profile. The range of variability in the continuum is directly related to the extent of the accretion footprints, with the models with the most localized accretion showing the most significant continuum modulation.

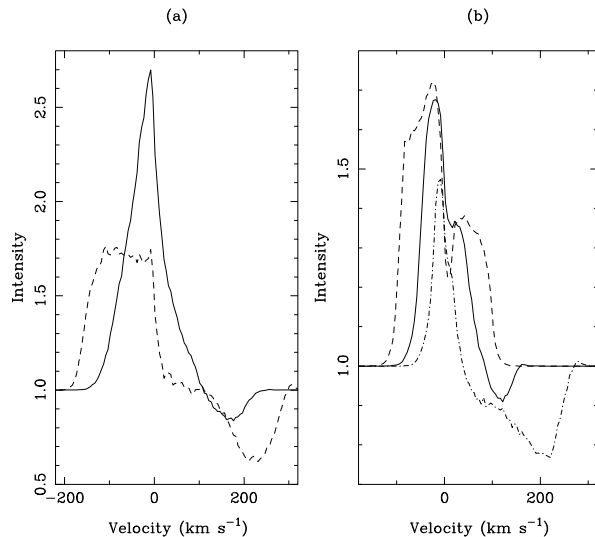


**Figure 5.**  $H\gamma$  spectra at selected phases. (a) D90 model (viewed at  $i = 60^\circ$ ) when curtains perpendicular to line of sight (phase 0.25; solid line) and along line of sight (phase 0; dashed line). (b) A30 model (viewed at  $i = 60^\circ$ ) with curtains perpendicular to line of sight (phase 0.25 or 0.75; solid line), with upper stream on far side of star (phase 0.5; dashed line) and with upper stream towards observer (phase 0; dot-dashed line).

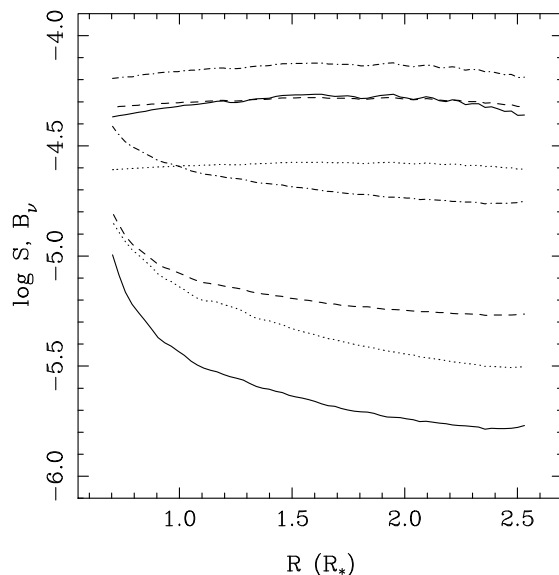


**Figure 6.** Source functions,  $S$ , for spectral lines in the accretion columns. Solid line:  $H\gamma$ ; dot-dashed:  $H\alpha$ ; dashed: Pa $\beta$ ; dotted: Br $\gamma$ . The local Planck function  $B_\nu$  is shown in the same style. For a given spectral line, the upper line shows  $B_\nu$  and the lower line shows  $S$ .

Although the mean spectrum can not be used to differentiate between different models, the time-series quotient spectra could be used as an observational diagnostic. The periodic behaviour of the lines is approximately similar in the three simulations, but the differing filling factors of the accretion flow produce different variations. When the nar-

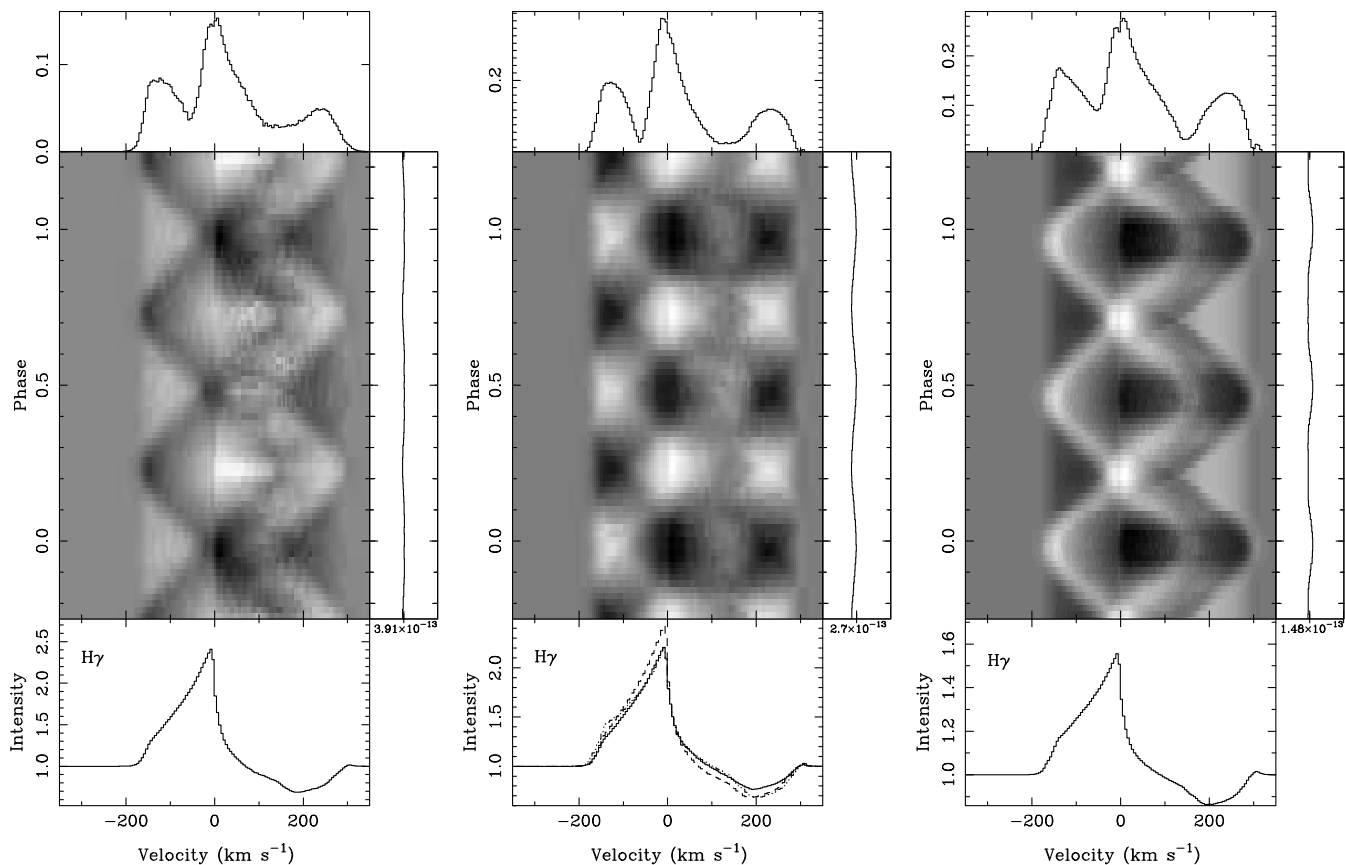


**Figure 7.**  $H\gamma$  spectra for three models viewed at  $60^\circ$  inclination, see Fig. 4 for a description. From left to right, D150, D90, D30. The variability shown in the greyscale has ranges of (from left to right) 39, 57 and 65 per cent of the mean spectrum in a given wavelength bin. The plot of the D90 mean spectrum (solid line) also shows the D150 (dashed line) and D30 (dotted line) mean spectra after they were all rescaled to have the same equivalent width.

rowest accretion flow, D30 (Fig. 2c)), is seen perpendicular to the line of sight (phase 0.25 or 0.75) there is very little gas projected against the hot-spots, and the line has only a small absorption at  $\sim 120 \text{ km s}^{-1}$ . At the same phases, the D150 model (Fig. 2a) creates an absorption feature at  $\sim 180 \text{ km s}^{-1}$  because the flow extends further in azimuth towards the observer and has components with higher projected velocity. The emission peak of the line profile shows equivalent behaviour for the same reason.

With only the accretion filling factor differing between the three models, the system’s rotation will average out the contribution from high and low projected gas velocities seen at different phases. It is therefore not surprising that the mean spectra differ only by a scaling factor. It is clear that observations of both line and continuum variability (that adequately sample the stellar rotation period) are needed to distinguish between the different geometries we have simulated here.

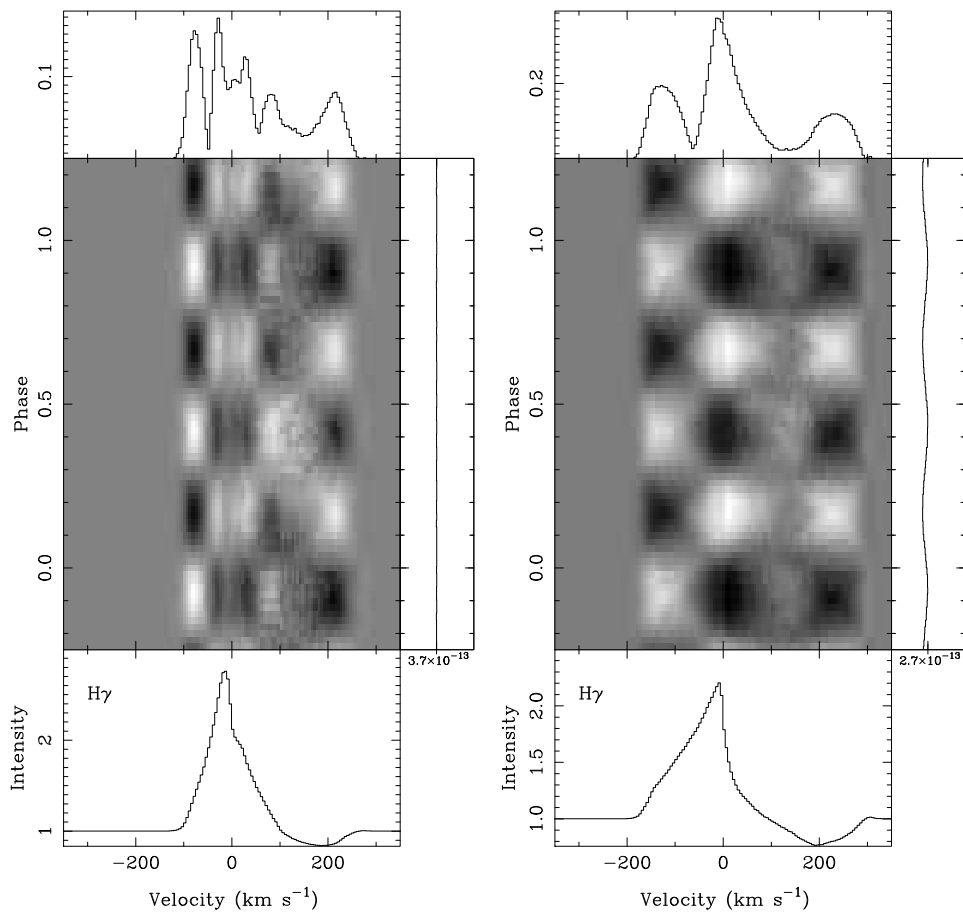
### 3.3 Inclination comparison

Fig. 8 shows the D90 model viewed at both  $30^\circ$  and  $60^\circ$  inclination. On average, the accretion streams have larger

velocity components parallel to the disc plane than perpendicular to it, so the line profile extends to higher velocities ( $-180$ – $300 \text{ km s}^{-1}$ ) at  $60^\circ$ , compared to  $30^\circ$  inclination ( $-120$ – $250 \text{ km s}^{-1}$ ). At  $30^\circ$  inclination, the continuum variation is comparable with the photon noise, but at  $60^\circ$  one of the upper accretion hot spots will not be visible at some phases and so the variability becomes significant (0.15 mag). Additionally, the two lower hotspots are never visible from  $30^\circ$ , but at  $60^\circ$  one of them will be seen at some phases.

The overall characteristics of the time-series quotient spectra are the same for both simulations, but the differences are clearly seen by inspection of the RMS variability spectra. At  $60^\circ$ , the line is varying at three distinct wavelength ranges, but a more complex pattern is seen at  $30^\circ$ . Some of the additional variability will be caused by the observer seeing (at some phases) through the inner disc hole to the high-velocity gas close to a lower accretion hotspot. In both simulations, there are lines-of-sight that view a lower (beneath the disc plane) accretion stream through an upper accretion stream. The projected velocity differences between the two streams is generally greater when viewed from  $30^\circ$  inclination, so this is also expected to create additional variability.





**Figure 8.**  $H\gamma$  spectra of the D90 model viewed at inclinations of  $30^\circ$  (left) and  $60^\circ$  (right). See Fig. 4 for a description. The variability shown in the greyscale has ranges of 35 (left) and 57 (right) per cent of the mean spectrum in a given wavelength bin.

### 3.4 Offset magnetic axis

Our A30 model is inspired by the MHD simulations of Romanova et al. (2003). The accretion streams are inclined by  $10^\circ$  with respect to the rotation axis, to represent a similarly inclined dipolar magnetic field (see Section 2.4). The accretion columns subtend  $30^\circ$  in azimuth and, unlike the other models, are not symmetric about their midplane. A stream exists above the disc plane on one side of the star, and below the disc plane on the opposite side (Fig. 2d). There are therefore only two hotspots on the stellar surface instead of the four that are present in the other models.

The line profile variability through a rotation period reflects the dramatic changes in the observer’s view of the gas flow (Figs. 9, 5b). The viewing angle of  $30^\circ$  (with respect to the disc normal and stellar rotation axes) keeps the upper accretion hotspot visible at all phases, but each gas flow is seen alternately towards, then away from the line of sight. Additionally, the lower stream suffers from varying occultation by the opaque accretion disc (affecting the low velocity component) and the stellar disc (blocking the high velocity component close to the obscured lower hotspot).

At phase 0.5 the upper stream is on the far side of the star and the lower stream is at maximum visibility through

the disc’s inner hole (Fig. 3c). All the hydrogen lines are composed of two distinct emission features – one redward of the rest wavelength and a larger one blueward. Material close to the disc with extremely low velocities is only seen in the upper stream and is visible throughout the rotation period so the line centre is not particularly variable. The varying presentation of the high-velocity gas in the upper stream dominates the quotient spectra of Fig. 9. Phase 0 sees the upper stream towards the observer, with its maximum projection onto the stellar disc. The blue continuum from the accretion hotspot is seen through the highest velocity gas and so the deepest wavelength bin in the redshifted absorption feature occurs at  $+210 \text{ km s}^{-1}$  in the  $H\gamma$  line. At  $\text{Br}\gamma$ , the unheated stellar surface contributes most of the continuum and the large volume of intermediate velocity gas seen over the star creates an absorption minimum at only  $+60 \text{ km s}^{-1}$ .  $H\alpha$  is not seen in absorption at any phase. There is a general trend for an enhancement of the line at two wavelengths, symmetrically about the rest wavelength, which moves alternately to lower and higher velocities through the rotation period.

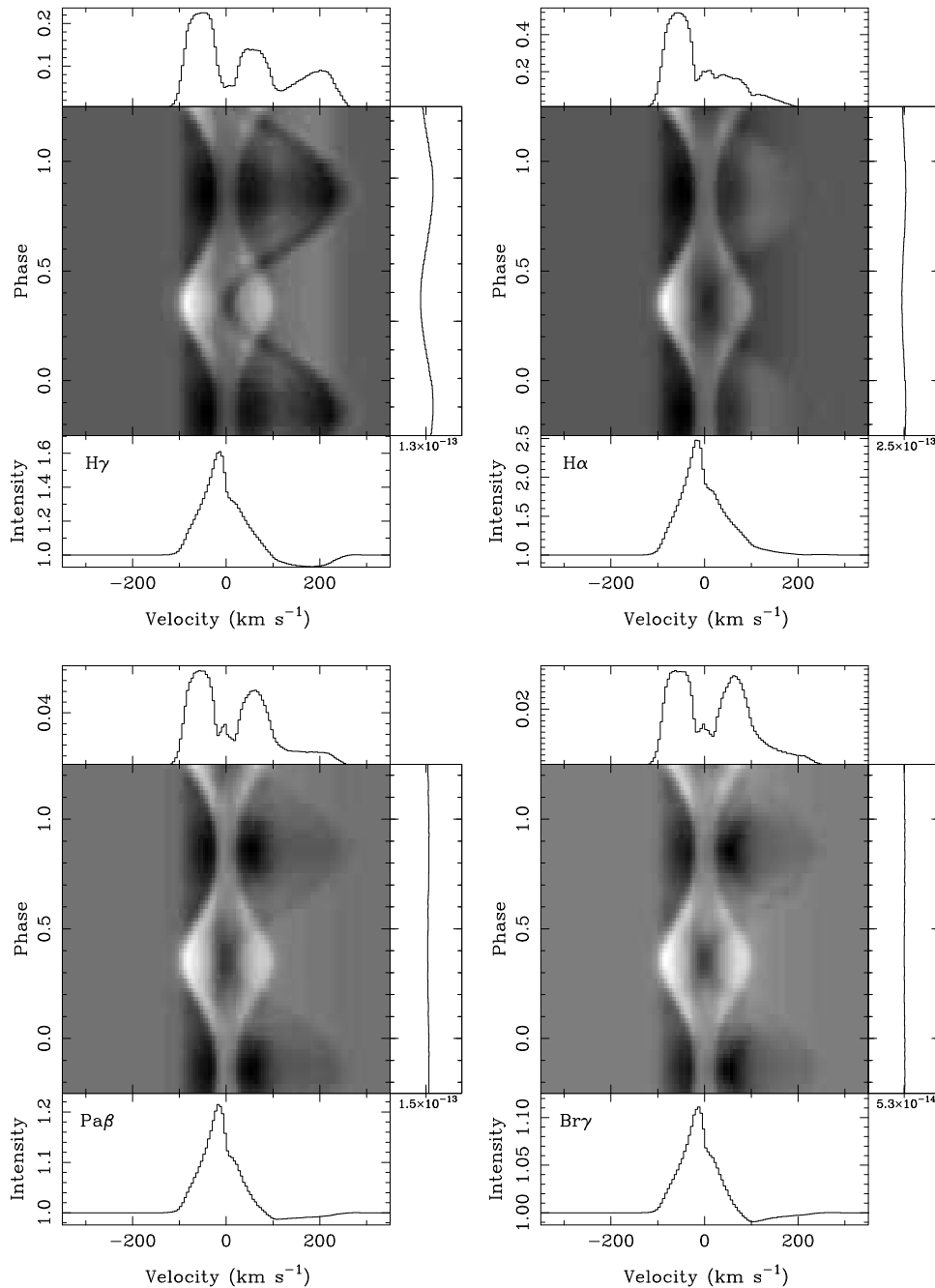


**Figure 9.** Spectra from A30 model, viewed at inclination of  $30^\circ$ . See Fig. 4 for a description. The variability shown in the greyscale has ranges (from top left) of 62, 112, 23 and 12 per cent of the mean spectrum in a given wavelength bin.

### 3.5 Correlation of variability

Observational studies of line profile variability in CTTS frequently use cross-correlation images to interpret the often complex phenomena that occur across profiles and between profiles from different transitions of species; a technique pioneered by Johns (1994) and Johns & Basri (1995a). We have computed auto-correlation (AC) images (see Figs. 10 and 11) for each line of our model time-series, following the method of Oliveira et al. (2000). The grey border of each image corresponds to the continuum, with white regions de-

scribing positive correlation and black features indicating negative correlation.

The  $H\gamma$  AC image for the D90 model at  $i = 60^\circ$  shows a region of positive correlation around the rest velocity of the line and at high redwards ( $200 - 250 \text{ km s}^{-1}$ ) and most bluewards ( $< 50 \text{ km s}^{-1}$ ) velocities. There is a ‘cross’ of low correlation centred on  $(+130, +130 \text{ km s}^{-1})$  and strong anticorrelation between the red side of the profile ( $0 - 250 \text{ km s}^{-1}$ ) and the blue side of the line ( $< -70 \text{ km s}^{-1}$ ). This anticorrelation is intrinsically linked to the diametric nature of the

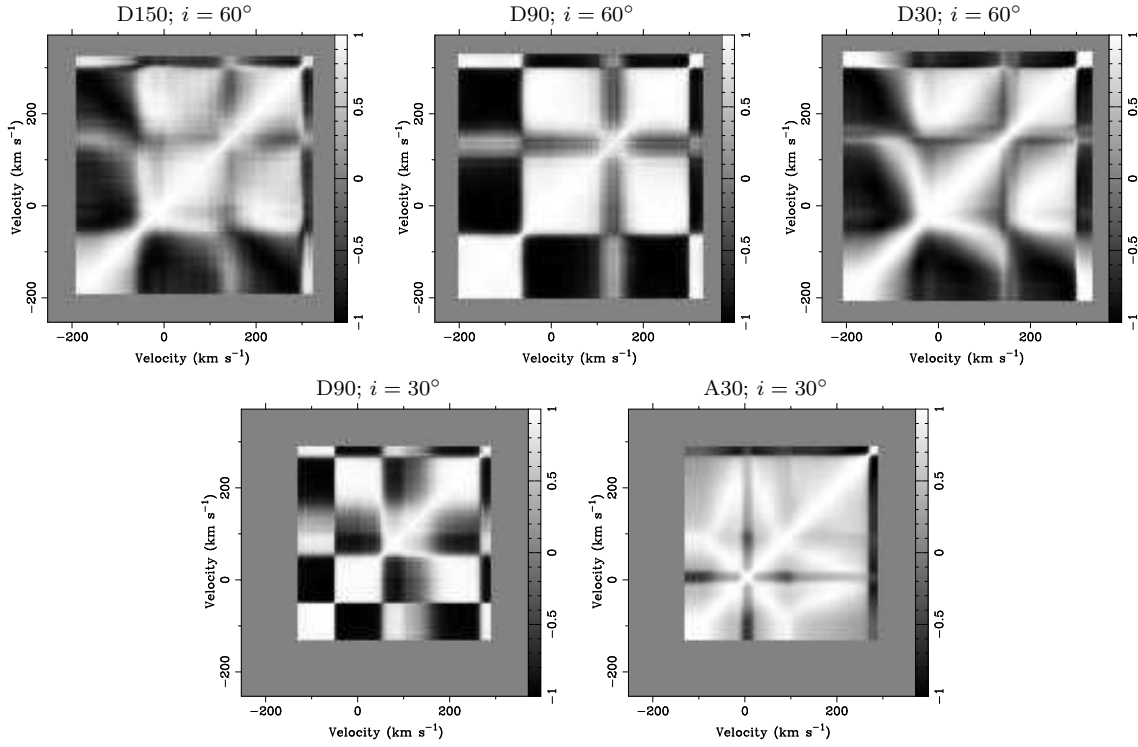


**Figure 10.** Images representing the auto-correlation function for the  $H\gamma$  line. The accretion model and the viewing inclination are shown above each image. The brightest shades represent the strongest correlation; the darkest shades are the strongest anti-correlations.

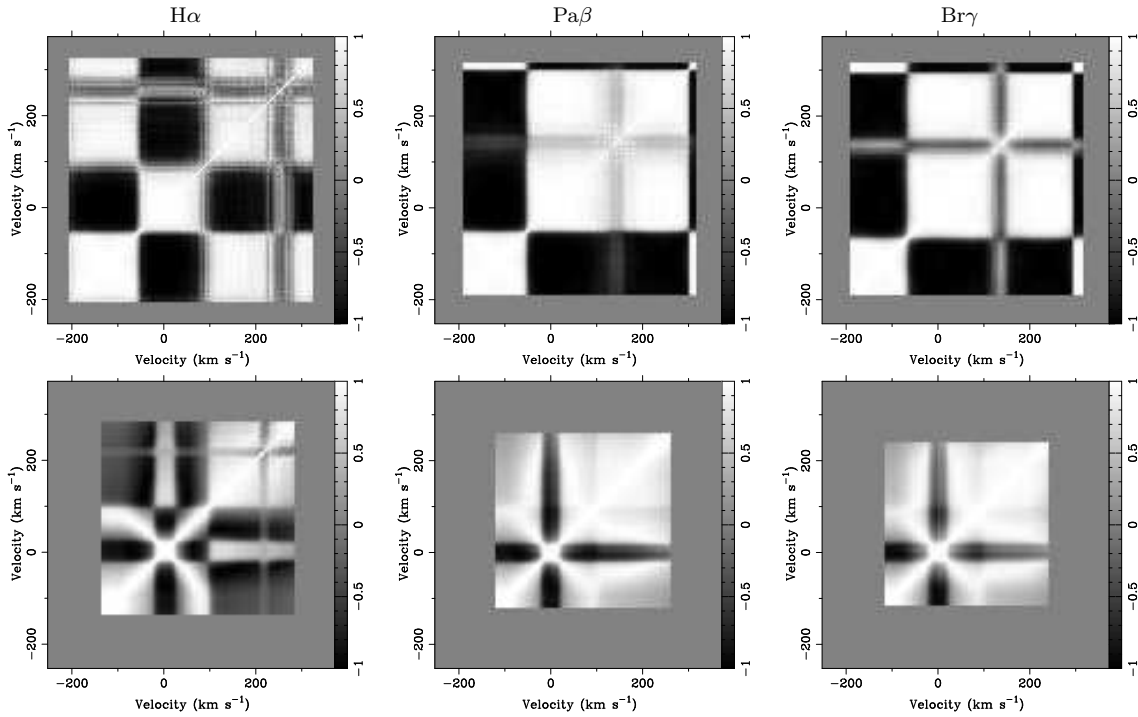


**Figure 11.** Images representing the auto-correlation function for some spectral lines. Top row: D90 model at  $60^\circ$  inclination; bottom row: A30 at  $30^\circ$  inclination. Within each row, the columns are, from left to right,  $H\alpha$ ,  $Pa\beta$  and  $Br\gamma$ . The brightest shades represent the strongest correlation; the darkest shades are the strongest anti-correlations.

accretion curtains: when one curtain is in front of the star (leading to enhanced absorption), the other is behind the star (leading to enhanced emission at blue velocities). The ‘cross’ is related to the D90 RMS spectra in Fig. 7, which shows a minimum at  $\sim +130 \text{ km s}^{-1}$ . The discontinuity between positive and negative correlation at  $\sim -70 \text{ km s}^{-1}$  corresponds to another minimum in the RMS spectra, and it can clearly be seen in the grayscale that the intensity varies in antiphase on either side of this velocity.

The D150 and D30 models at  $60^\circ$  inclination have similar features, and so do the D90 models in the near infrared Pa $\beta$  and Br $\gamma$  lines. The D90 H $\alpha$  line has an anti-correlation region between the rest velocity and velocities greater than  $+100 \text{ km s}^{-1}$ ; this additional feature arises because H $\alpha$  is the only line in the D90  $i = 60^\circ$  model that does not show an IPC profile. The same effect is seen in the H $\alpha$  line of the A30 model, whose other lines are positively auto-correlated over most of their wavelength ranges.

We have also computed cross-correlation (CC) images (with zero lag) of the H $\alpha$  profiles with the H $\gamma$  profiles for each of our models (Fig. 12). For the D90 model the cross-correlation image demonstrates that the variability in the red sides of the H $\alpha$  and H $\gamma$  profiles is anticorrelated. This anticorrelation is directly visible in the grayscale images of Fig. 4, with bright features (excess emission) on the red side of H $\alpha$  coinciding with increased absorption in H $\gamma$ . A similar pattern is seen for the D150 and D30 CC images. The A30 CC image shows that the red wing of the H $\alpha$  profile is anticorrelated with practically the whole H $\gamma$  line. This is a consequence of the red wing varying for only fraction of the rotation period – the same range of phases at which the upper hotspot is visible and suppressing the emission line.

## 4 DISCUSSION

The illustrative models presented in this paper represent a first step in quantifying the emission line profile variability observed in CTTS. We did not adjust the simulation parameters to achieve agreement with any existing data, and our choice of simple configurations has produced line profiles with high levels of variation. It is therefore most useful to consider the general characteristics seen in our time-series spectra.

Our synthetic spectra typically predict levels of line profile variability that are significantly greater than those observed. Only the D150 model, which has wide accretion curtains, shows variability that is comparable to published data e.g. Smith et al. (2001). The geometry with the least symmetry (A30) leads to line profiles that change substantially in shape and intensity from one rotation phase to another. This geometry was selected to represent the structures indicated by recent MHD calculations (Romanova et al. 2003), but it appears that the line profiles predicted by such a magnetosphere are sufficiently at odds with spectroscopic observations that this form of MHD model may be rejected.

MHD simulations must balance the interactions of the accretion disk with a magnetic field that includes large scale structure (e.g. a dipolar component) with local irregularities. Both accretion flows onto the star and magnetically launched outflows (e.g. Miller & Stone 1997) must be derived self-consistently to explain observed spectral features.

CTTSs are probably more fully enveloped in accreting gas than our A30 model proposes, but equally, the broad symmetric curtains of our D150 and D90 models are too regular to represent the circumstellar environment. Better agreement might have been reached by keeping the high density streams, but elsewhere setting a lower mass accretion rate that would increase the azimuthal filling factor of the magnetosphere.

The RMS spectra of our simulations often show several distinct minima, corresponding to velocities where the emission from line-of-sight iso-velocity surfaces remains constant. This pattern of variability is not often seen in the observations, although H $\alpha$ , H $\beta$ , and NaI doublet variance profiles of SU Aur (Oliveira et al. 2000) do show multiple regions of minimum variability. More typically the line variability is most pronounced either on the red (Smith et al. 2001) or blue (Alencar et al. 2001) sides of the profile. Occasionally a bimodal distribution of variability is seen across the emission lines, with equal variability in the red- and blue-line-wings and a minimum at the line centre (Alencar & Batalha 2002). Given that our models neglect any outflow component, our RMS spectra typically indicate strongest variability on the red side of the model profiles. However the A30 model, with its narrow curtains, shows that blue-side line variability can be dominant (particularly at H $\alpha$ ) even with an infall geometry.

Cross- and auto-correlation images are widely used as a diagnostic of line profile variability in CTTS (e.g. Johns & Basri 1995a; Oliveira et al. 2000; Alencar et al. 2001; Alencar & Batalha 2002). A square, cross-shaped auto-correlation function is often seen in the lower-order Balmer lines (e.g. Johns & Basri 1995a; Alencar & Batalha 2002; Oliveira et al. 2000) and this has been interpreted as resulting from viewing the the magnetosphere at low inclinations (Alencar & Batalha 2002). We find such a pattern in our AC images for essentially all our models (see Figs. 10, 11), indicating that the AC images may be of limited diagnostic potential. The cross-correlation images at zero lag (see Fig. 12) show a variety of structures, but we find no obvious similarities with the published CC images.

Interestingly, while the variability of the emission line profiles in our simulations is excessive, the ranges of continuum flux (Table 1) are comparable with, or even lower than, results from photometric surveys, where  $V$  band magnitudes are seen to change periodically by up to  $\sim 1$  mag (e.g. Bouvier et al. 1993). In the models presented here, any smoothing of the azimuthal magnetospheric structure (broadening of the curtains for example) in order to reduce line profile variability, will lead to an equal smoothing of the surface hot spots (and a corresponding reduction in continuum variability). The simultaneous satisfaction of the dual spectroscopic and photometric observational constraints represents a challenging problem.

## 5 CONCLUSIONS AND FUTURE WORK

We have presented the first 3D radiative transfer calculations of non-axisymmetric accretion onto classical T Tauri stars. Hydrogen line profiles throughout the stellar rotation period are shown for three systems that have accretion confined to curtains filling part of a dipolar magnetosphere.

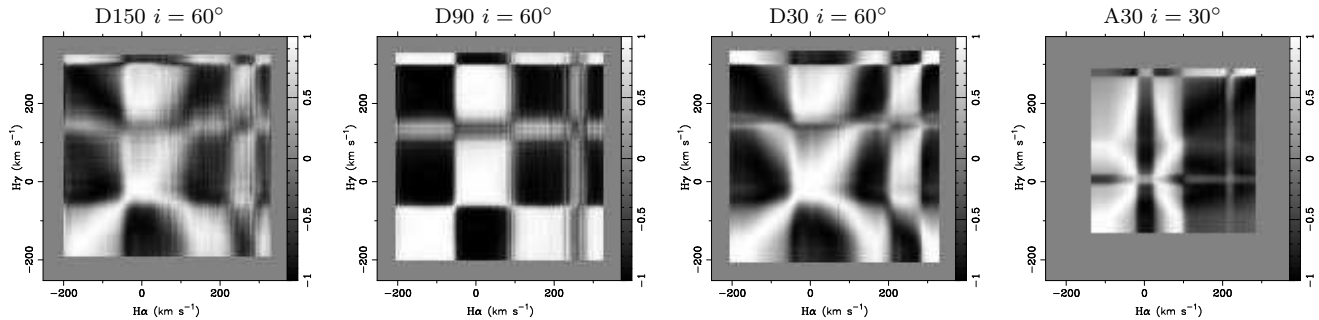


**Figure 12.** Cross-correlation maps for the  $H\alpha$  and  $H\gamma$  spectral lines in the four accretion models. The model and the viewing inclination are shown above each image. The brightest shades represent the strongest correlation; the darkest shades are the strongest anti-correlations.

Three of the models had curtains that were symmetric about the disc plane, and the fourth accreted from above the disc on one side of the star, and from below on the other side. The latter configuration was suggested by MHD simulations of stars with an inclined dipolar field, but we find that our model creates line profiles that are excessively variable when compared to observations. We suggest that CTTS magnetospheres may have high filling factors of accreting gas, but with local enhancements that may be in the form of streams confined in azimuth.

The simple models presented here are, of course, unable to reproduce the wide range of variable phenomenon observed. Nonetheless, some gross characteristics of the line profile variability are reflected in the models, including the form of the variability's velocity distribution and the auto-correlation images. In the future we will investigate the line and continuum diagnostics of non-static accretion models. Time-series spectroscopy of AA Tau by Bouvier et al. (2003) already hints at changes in the global accretion rate on a time-scale of hours. Using a simple freefall model we should be able to examine how a change in the mass-accretion rate affects the line profiles and continuum flux as it propagates down the field lines. Our self-consistent model for the reprocessed accretion power should enable us to determine the lag between the line and continuum variability.

Furthermore, the observation of anticorrelation between the blue and red side variability of  $H\alpha$  in SU Aur has been interpreted using a dipole offset model with simultaneous dipolar accretion and an outflow (Johns & Basri 1995b). The inclusion of a wind component in our geometry will enable us to investigate such scenarios and make quantitative predictions regarding the line variability.

Finally, the TORUS code includes computation of the Stokes vectors for the simulated photon packets, and can measure linear polarization by scattering events. Addition of a magnetic field configuration to our simulation grid would allow circular spectropolarimetry to be simulated. This technique has already been used observationally to show CTTS emission lines originate in structures with a net magnetic field (Johns-Krull et al. 1999; Symington et al. 2005), so self-consistent modelling of line intensity and polarization would allow more stringent tests of magnetospheric accretion models.

## ACKNOWLEDGEMENTS

RK is funded by PPARC standard grant PPA/G/S/2001/00081.

## REFERENCES

- Alencar S. H. P., Basri G., 2000, *AJ*, 119, 1881  
 Alencar S. H. P., Batalha C., 2002, *ApJ*, 571, 378  
 Alencar S. H. P., Johns-Krull C. M., Basri G., 2001, *AJ*, 122, 3335  
 Armitage P. J., Clarke C. J., 1996, *MNRAS*, 280, 458  
 Basri G., 1990, *Memorie della Societa Astronomica Italiana*, 61, 707  
 Bertout C., 1989, *ARA&A*, 27, 351  
 Bouvier J., Cabrit S., Fernandez M., Martin E. L., Matthews J. M., 1993, *A&A*, 272, 176  
 Bouvier J., Grankin K. N., Alencar S. H. P., Dougados C., Fernández M., Basri G., Batalha C., Guenther E., Ibrahimov M. A., Magakian T. Y., Melnikov S. Y., Petrov P. P., Rud M. V., Zapatero Osorio M. R., 2003, *A&A*, 409, 169  
 Choi P. I., Herbst W., 1996, *AJ*, 111, 283  
 Collier Cameron A., Campbell C. G., 1993, *A&A*, 274, 309  
 Decampli W. M., 1981, *ApJ*, 244, 124  
 Edwards S., Hartigan P., Ghandour L., Andrusis C., 1994, *AJ*, 108, 1056  
 Harries T. J., 1995, Ph.D. Thesis, Univ. of London  
 Harries T. J., 2000, *MNRAS*, 315, 722  
 Harries T. J., Monnier J. D., Symington N. H., Kurosawa R., 2004, *MNRAS*, 350, 565  
 Hartmann L., 1998, *Accretion processes in star formation*. Cambridge University Press. (Cambridge astrophysics series; 32)  
 Hartmann L., 2002, *ApJ*, 566, L29  
 Hartmann L., Avrett E., Edwards S., 1982, *ApJ*, 261, 279  
 Hartmann L., Hewett R., Calvet N., 1994, *ApJ*, 426, 669  
 Johns C. M., 1994, Ph.D. Thesis, Univ. California  
 Johns C. M., Basri G., 1995a, *AJ*, 109, 2800  
 Johns C. M., Basri G., 1995b, *ApJ*, 449, 341  
 Johns-Krull C. M., Valenti J. A., Hatzes A. P., Kanaan A., 1999, *ApJ*, 510, L41  
 Klein R. I., Castor J. I., 1978, *ApJ*, 220, 902  
 Koenigl A., 1991, *ApJ*, 370, L39  
 Kurosawa R., Harries T. J., Bate M. R., Symington N. H., 2004, *MNRAS*, 351, 1134  
 Kurosawa R., Hillier D. J., 2001, *A&A*, 379, 336

- Kurucz R., 1993, Kurucz CD-ROM No. 13. Smithsonian Astrophysical Observatory
- Lawson W. A., Lyo A.-R., Muzerolle J., 2004, MNRAS, 351, L39
- Martin S. C., 1996, ApJ, 470, 537
- Miller K. A., Stone J. M., 1997, ApJ, 489, 890
- Muzerolle J., Calvet N., Hartmann L., 1998, ApJ, 492, 743
- Muzerolle J., Calvet N., Hartmann L., 2001, ApJ, 550, 944
- Muzerolle J., Hillenbrand L., Calvet N., Briceño C., Hartmann L., 2003, ApJ, 592, 266
- Oliveira J. M., Foing B. H., van Loon J. T., Unruh Y. C., 2000, A&A, 362, 615
- Paatz G., Camenzind M., 1996, A&A, 308, 77
- Petrov P. P., Gullbring E., Ilyin I., Gahm G. F., Tuominen I., Hackman T., Loden K., 1996, A&A, 314, 821
- Romanova M. M., Ustyugova G. V., Koldoba A. V., Wick J. V., Lovelace R. V. E., 2003, ApJ, 595, 1009
- Shu F., Najita J., Ostriker E., Wilkin F., Ruden S., Lizano S., 1994, ApJ, 429, 781
- Smith K., Lewis G. F., Bonnell I. A., Emerson J. P., 2001, A&A, 378, 1003
- Smith K. W., Lewis G. F., Bonnell I. A., Bunclark P. S., Emerson J. P., 1999, MNRAS, 304, 367
- Stassun K. G., Mathieu R. D., Mazeh T., Vrba F. J., 1999, AJ, 117, 2941
- Steinacker J., Henning T., Bacmann A., Semenov D., 2003, A&A, 401, 405
- Stempels H. C., Piskunov N., 2002, A&A, 391, 595
- Symington N. H., 2005, Ph.D. Thesis, Univ. of Exeter
- Symington N. H., Harries T. J., Kurosawa R., 2005, MNRAS, submitted
- Valenti J. A., Johns-Krull C. M., Hatzes A. P., 2003, in A. Brown, G.M. Harper, T.R. Ayres, eds, 12th Cambridge Workshop on Cool Stars, Stellar Systems, and the Sun (University of Colorado) . p. 729